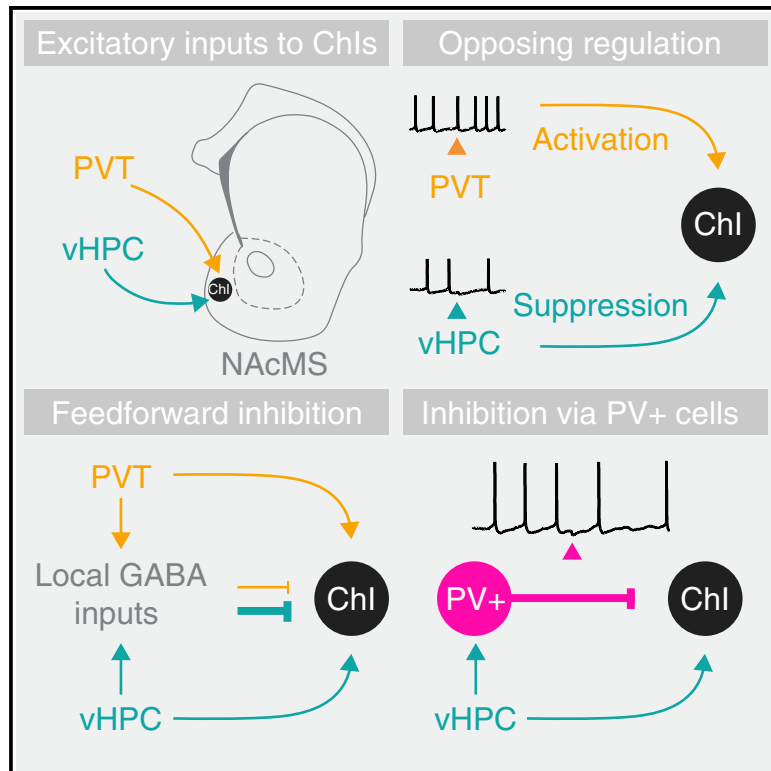


Hippocampal-evoked inhibition of cholinergic interneurons in the nucleus accumbens

Graphical abstract



Authors

Corey Baimel, Emily Jang, Samantha L. Scudder, Kasra Manoocheri, Adam G. Carter

Correspondence

adam.carter@nyu.edu

In brief

Baimel et al. examine the afferent control of cholinergic interneurons (ChIs) in the nucleus accumbens medial shell (NAcMS). Inputs from the ventral hippocampus (vHPC) and paraventricular nucleus of the thalamus have opposing influence on ChI firing. vHPC-evoked inhibition reflects activation of parvalbumin (PV+) interneurons, which robustly inhibit ChIs in NAcMS.

Highlights

- NAcMS ChIs receive excitatory inputs from the vHPC and PVT
- PVT inputs enhance, but vHPC inputs pause, ongoing firing of ChIs
- vHPC-evoked pauses are due to robust feedforward inhibition onto ChIs
- PV+ cells mediate vHPC-evoked feedforward inhibition of ChIs in the NAcMS



Report

Hippocampal-evoked inhibition of cholinergic interneurons in the nucleus accumbens

Corey Baimel,¹ Emily Jang,¹ Samantha L. Scudder,¹ Kasra Manoocheri,¹ and Adam G. Carter^{1,2,*}¹Center for Neural Science, New York University, 4 Washington Place, New York, NY 10003, USA²Lead contact*Correspondence: adam.carter@nyu.edu<https://doi.org/10.1016/j.celrep.2022.111042>**SUMMARY**

Cholinergic interneurons (ChIs) in the nucleus accumbens (NAc) play a central role in motivated behaviors and associated disorders. However, while the activation of ChIs has been well studied in the dorsal striatum, little is known about how they are engaged in the NAc. Here, we find that the ventral hippocampus (vHPC) and the paraventricular nucleus of the thalamus (PVT) are the main excitatory inputs to ChIs in the NAc medial shell. While the PVT activates ChIs, the vHPC evokes a pronounced pause in firing through prominent feed-forward inhibition. In contrast to the dorsal striatum, this inhibition reflects strong connections onto ChIs from local parvalbumin interneurons. Our results reveal the mechanisms by which different long-range inputs engage ChIs, highlighting fundamental differences in local connectivity across the striatum.

INTRODUCTION

Cholinergic interneurons (ChIs) represent only a small percentage of striatal neurons but exert profound influence on striatal function. They are the main source of striatal acetylcholine and regulate striatal output through multiple mechanisms, including recruitment of disinaptic inhibition onto medium spiny neurons (MSNs) (Assous et al., 2017; English et al., 2011; Koós and Tepper, 2002) and modulation of dopamine and glutamate release (Cachope et al., 2012; Higley et al., 2009; Kosillo et al., 2016; Liu et al., 2022; Malenka and Kocsis, 1988; Shin et al., 2015; Sugita et al., 1991; Threlfell et al., 2012). Although ChIs are tonically active (Brown et al., 2012; Virk et al., 2016; Wilson et al., 1990; Witten et al., 2010), they display dynamic shifts in firing, with environmental cues that discourage or promote action able to transiently engage or suppress ChI activity and signaling (Howe et al., 2019; Mark et al., 1992; Nougaret and Ravel, 2015), and optogenetic activation of ChIs during cue presentation sufficient to prevent behavioral action (Collins et al., 2019). ChIs also exhibit phasic pauses in firing following salient reward-predicting cues (Aosaki et al., 1994; Apicella et al., 2009; Ravel et al., 2003; Zhang and Cragg, 2017), which are sufficient to enhance stimulus-outcome learning (Al-Hasani et al., 2021; Brown et al., 2012; Vachez et al., 2021). Moreover, ChI activity is linked to drug addiction (Lee et al., 2016; Witten et al., 2010) and depressive-like behaviors (Warner-Schmidt et al., 2012). Given their broad roles in controlling striatal activity, function, and disease, it is important to understand the factors governing ChI activity.

In the dorsal striatum, long-range excitatory inputs from the cortex and thalamus activate ChIs (Ding et al., 2010; Doig et al., 2014; Lapper and Bolam, 1992), but the equivalent regulation of ChIs in the nucleus accumbens (NAc) is much less explored. Recent ev-

idence highlights a role for inhibitory inputs from the ventral pallidum and the ventral tegmental area in controlling ChI activity (Al-Hasani et al., 2021; Brown et al., 2012), but the NAc also receives and integrates excitatory inputs from other brain regions, including the prefrontal cortex, paraventricular nucleus of the thalamus, ventral hippocampus, and amygdala (Britt et al., 2012; Phillipson and Griffiths, 1985; Sesack and Grace, 2010). These inputs make strong synaptic connections onto MSNs and engage distinct networks to coordinate motivated behavior (Ambroggi et al., 2008; Baimel et al., 2019; Britt et al., 2012; MacAskill et al., 2012, 2014; Pascoli et al., 2014; Reed et al., 2018; Scudder et al., 2018), but the degree to which they influence neighboring ChIs is unknown. Here, we use a combination of whole-brain rabies tracing, whole-cell patch-clamp electrophysiology, and optogenetics to study how long-range excitatory inputs modulate the activity of ChIs in the mouse NAc medial shell (NAcMS). We show input-specific regulation of the firing properties of ChIs, with pronounced hippocampal-evoked feedforward inhibition (FFI) that is mediated via parvalbumin interneurons.

RESULTS**Ventral hippocampus and paraventricular nucleus of the thalamus are the main excitatory inputs to ChIs in the NAcMS**

We first mapped the brain-wide innervation of ChIs in the NAcMS using monosynaptic input tracing with a conditional rabies virus in ChAT-Cre mice (Wall et al., 2010). We injected adeno-associated virus (AAV)-FLEX-TVA-mCherry and AAV-FLEX-oG into the NAcMS, waited 5 weeks for expression, and then injected SAD-ΔG-GFP pseudotyped rabies virus (EnvA-RV-GFP) in the same location to infect TVA + oG-expressing ChIs (Figure 1A). While starter cells were restricted to the NAcMS (Figure 1A), input



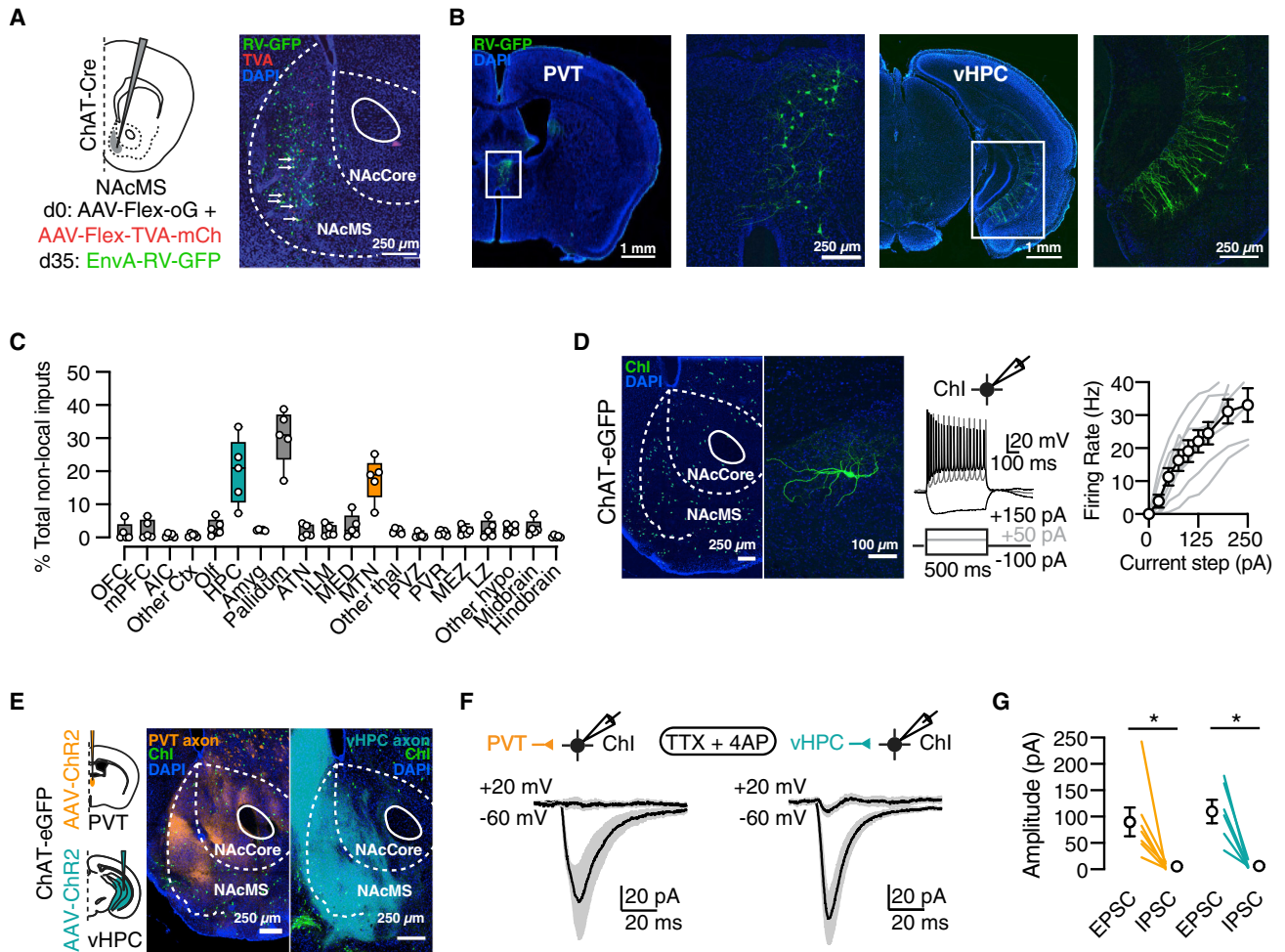


Figure 1. ChIs receive excitatory inputs from the PVT and vHPC

(A) Left: schematic and protocol for monosynaptic rabies tracing in ChAT-Cre mice. Right: example image of starter cells (white arrows) and local input neurons (green) in the NAcMS.

(B) Example images of presynaptic neurons in the PVT and vHPC, where boxed regions are expanded.

(C) Summary of the distribution of non-local input neurons throughout the brain ($n = 5$ mice). OFC, orbitofrontal cortex; mPFC, medial prefrontal cortex; AIC, agranular insular cortex; Other ctx, other cortex; Olf, olfactory areas, HPC, hippocampal formation, Amyg, amygdala, ATN, anterior dorsal thalamus; ILM, intralaminar dorsal thalamus; MED, medial dorsal thalamus; MTN, midline dorsal thalamus, Other thal, other thalamic nuclei; PVZ, periventricular zone of hypothalamus; PVR, periventricular region of hypothalamus; MEZ, medial hypothalamus; LZ, lateral hypothalamus; Other hypo, other hypothalamus.

(D) Left: example image showing distribution of ChIs in the NAcMS of ChAT-EGFP mice. Middle: example of a ChI in the NAcMS. Right: physiological responses of ChIs to brief current injections and summary of firing (F) versus current (I) curves, showing ChIs can be readily driven to fire ($n = 9$ cells/3 mice).

(E) Injection schematic and examples of axon labeling in the NAcMS for injections of AAV-ChR2 in the PVT (orange) or the vHPC (teal) of ChAT-EGFP mice.

(F) Both PVT (left) and vHPC (right) make monosynaptic excitatory connections onto ChIs. Voltage-clamp recordings of ChIs in the presence of TTX + 4-AP reveal light-evoked EPSCs at -60 mV but not IPSCs at $+20$ mV (PVT: $n = 7$ cells/4 mice; vHPC: $n = 7$ cells/3 mice).

(G) Summary of EPSC and IPSC amplitudes for PVT (orange) and vHPC (teal) terminal stimulation, where lines indicate individual neurons.

Box and whisker plots represent median and minimum to maximum. Average traces, current amplitude data, and F-I curve are presented as mean \pm SEM. * $p < 0.05$.

See also Figure S1.

neurons were observed across the rostral-caudal axis of the brain ($n = 6,534$ cells from 5 mice, $1,307 \pm 309$ cells) (Figure S1). Presynaptic cells included a dense array of local NAcMS neurons ($n = 2,686$ total cells from 5 mice, 537 ± 108 cells, $43\% \pm 4\%$ of presynaptic neurons), as well as non-local neurons ($n = 3,848$ total cells from 5 mice, 770 ± 229 cells, $57\% \pm 4\%$ of presynaptic neurons) (Figure S1). Amongst the non-local neurons,

the densest labeling was observed in the anterior portion of the midline dorsal thalamus ($18\% \pm 3\%$ of non-local inputs), including the paraventricular nucleus of the thalamus (PVT) ($50\% \pm 4\%$ of midline dorsal thalamic inputs), throughout the ventral hippocampus (vHPC) ($20\% \pm 4\%$ of non-local inputs), and the anterior portion of the ventral pallidum ($31\% \pm 4\%$ of non-local inputs) (Figures 1B, 1C, and S1).

Our rabies data identify which upstream regions contact ChIs but not the sign and strength of these connections. Although the ventral pallidum contains both glutamatergic and GABAergic projection neurons (Faget et al., 2018; Tooley et al., 2018), recent studies show that it is an important inhibitory input to NAc ChIs (Vachez et al., 2021). On the other hand, the PVT and vHPC represent two glutamatergic inputs to the NAc that are known to strongly contact MSNs in the NAcMS (Baimel et al., 2019; Britt et al., 2012; Christoffel et al., 2021; MacAskill et al., 2012, 2014; Zhu et al., 2016) but whose connections with ChIs have not been examined. We thus focused on the regulation of ChIs by the PVT and vHPC. Using ChAT-eGFP mice, we visualized ChIs by their green fluorescence, showing a sparse population of large neurons with thick aspiny dendrites and intrinsic properties similar to ChIs in the dorsal striatum (Figure 1D) (Straub et al., 2014). To study connections onto ChIs, we next injected AAV-CaMKII-ChR2 into either the PVT or vHPC, which led to characteristic axonal profiles in the NAcMS (Figure 1E). We then performed *ex vivo* whole-cell voltage-clamp recordings where we activated PVT or vHPC inputs with blue (470 nm) light and examined excitatory and inhibitory synaptic connections by holding ChIs at -60 ($E_{\text{GABA}_A\text{-R}}$) and $+20$ mV ($E_{\text{AMPA}\text{-R}}$), respectively, in the presence of the NMDA receptor (NMDAR) antagonist CPP (10 μM). We also isolated monosynaptic connections by including tetrodotoxin (TTX; 1 μM), 4-AP (0.1 mM), and 4 mM Ca^{2+} in the bath solution (Little and Carter, 2013; Petreanu et al., 2009). For both PVT and vHPC inputs, we observed robust excitatory postsynaptic currents (EPSCs) (PVT: 90 ± 27 pA, $n = 7$ cells/4 mice; vHPC: 108 ± 22 pA, $n = 7$ cells/3 mice) but not inhibitory postsynaptic currents (IPSCs) (PVT: 6 ± 2 pA, vHPC: 5 ± 2 pA; PVT-evoked EPSC versus IPSC amplitude: Wilcoxon test: $W = -28$, $p = 0.02$; vHPC-evoked EPSC versus IPSC amplitude: Wilcoxon test: $W = -21$, $p = 0.03$) (Figures 1F and 1G), confirming direct excitatory connections onto ChIs. Together, these findings indicate that ChIs in the NAcMS receive prominent excitatory inputs from both the PVT and vHPC, suggesting connections from these areas may functionally enhance ChI activity.

PVT inputs excite ChIs, but vHPC inputs pause their firing

Having identified the main excitatory inputs to ChIs in the NAcMS, we next examined their impact on ChI activity. We monitored action-potential firing from spontaneously active ChIs in the NAcMS with whole-cell current-clamp recordings. ChIs were sufficiently depolarized to maintain baseline firing around 5 Hz, similar to levels recorded *in vivo* (Wilson et al., 1990). To investigate whether PVT and vHPC inputs induce similar changes in ChI activity, we again expressed ChR2 in the PVT or vHPC of ChAT-eGFP mice. For PVT inputs, a brief flash of blue light (2 ms, 10 mW, 470 nm) induced an immediate and transient increase in firing ($n = 8$ cells/6 mice) (Figure 2A), quantified by an increase in spike probability (mean = 5.4-fold increase, 10 ms time bin from the stimulation) that quickly returned to baseline (Friedman test: $F = 10.89$, $p = 0.003$) (Figure 2B), with no change in inter-spike interval following stimulation (baseline [BL]: 358 ± 66 ms, stimulation [Stim]: 338 ± 49 ms; Wilcoxon test: $W = 3.0$, $p = 0.9$) (Figure 2C). In contrast,

equivalent activation of vHPC inputs induced robust silencing of tonic firing in ChIs ($n = 11$ cells/9 mice) (Figure 2A). In some recordings, the evoked pause in firing was preceded by an acute increase in spiking immediately after light stimulation (mean = 2.2-fold increase). However, the predominant effect was a delayed and prolonged pause in firing (Friedman test: $F = 13.64$, $p = 0.0004$) (Figure 2B), which was marked by a pronounced increase in the inter-spike interval after light stimulation (BL: 289 ± 34 ms, Stim: 428 ± 66 ms; Wilcoxon test: $W = 58.0$, $p = 0.007$) (Figure 2C). Together, these results suggest that the two main glutamatergic inputs to ChIs in the NAcMS evoke distinct, bidirectional modulation of action-potential discharge of ChIs.

We were intrigued by the vHPC-evoked suppression of firing in ChIs, which could be evoked through intrinsic or synaptic mechanisms. In separate experiments, we confirmed that strong activation through brief, depolarizing current steps was sufficient to drive a brief increase and subsequent pause in the firing in ChIs (Figure S2). However, the vHPC-evoked pause occurred in the absence of a robust increase in spiking, so we suspected a synaptic mechanism was likely the source of the pause. Although the vHPC makes direct excitatory connections in the NAcMS, it also engages FFI (Scudder et al., 2018). We thus hypothesized that the vHPC-induced suppression of firing may result from vHPC-driven inhibition via the local circuit. We repeated these experiments with inclusion of gabazine or NBQX in the bath to block GABA_A or AMPA receptors, respectively (Figure 2A). Recording in gabazine revealed an excitatory effect of vHPC terminal stimulation, quantified by an increase in spike probability (mean = 4.2 fold increase; Friedman test: $F = 8.63$, $p = 0.01$; $n = 7$ cells/3 mice) (Figure 2B), but no effect on inter-spike interval (BL: 281 ± 25 ms, Stim: 274 ± 40 ms; Wilcoxon test: $W = -5.0$, $p = 0.8$) (Figure 2C), akin to what we observed for PVT stimulation. Including gabazine did not alter PVT-evoked activity in ChIs (Figure S2). In contrast, both vHPC-evoked excitation and suppression of firing were blocked by NBQX (normalized spike probability, Friedman test: $F = 2.0$, $p = 0.5$; $n = 7$ cells/3 mice; inter-spike interval, BL: 275 ± 20 ms, Stim: 293 ± 32 ms; Wilcoxon test: $W = 14.0$, $p = 0.3$) (Figures 2A–2C), which abolishes both direct excitation and the recruitment of local interneurons. Together, these results suggest that PVT and vHPC inputs differentially engage mono- and disynaptic circuits to modulate ChIs, with vHPC evoking FFI.

vHPC inputs engage robust FFI onto ChIs

Our current-clamp data suggest differential recruitment of FFI onto ChIs by the PVT and vHPC. To directly test this idea, we next performed voltage-clamp recordings in ChIs, measuring PVT- and vHPC-evoked EPSCs and IPSCs in the absence of TTX and 4-AP, which allows for polysynaptic activity in the circuit. With brief activation of PVT inputs (2 ms, 2–10 mW, 470 nm), we observed EPSCs at -60 mV, which were similar in amplitude to delayed IPSCs at $+20$ mV ($n = 7$ cells/4 mice; EPSC amplitude: 48 ± 11 pA, IPSC amplitude: 59 ± 23 pA; Wilcoxon test: $W = 5.0$, $p = 0.82$; EPSC onset: 2.8 ± 0.2 ms, IPSC onset: 7.0 ± 0.5 ms; Wilcoxon test: $W = 36$, $p = 0.008$) (Figures 3A and S3). Although small in amplitude, this targeting was specific to ChIs, as more robust EPSCs and IPSCs were

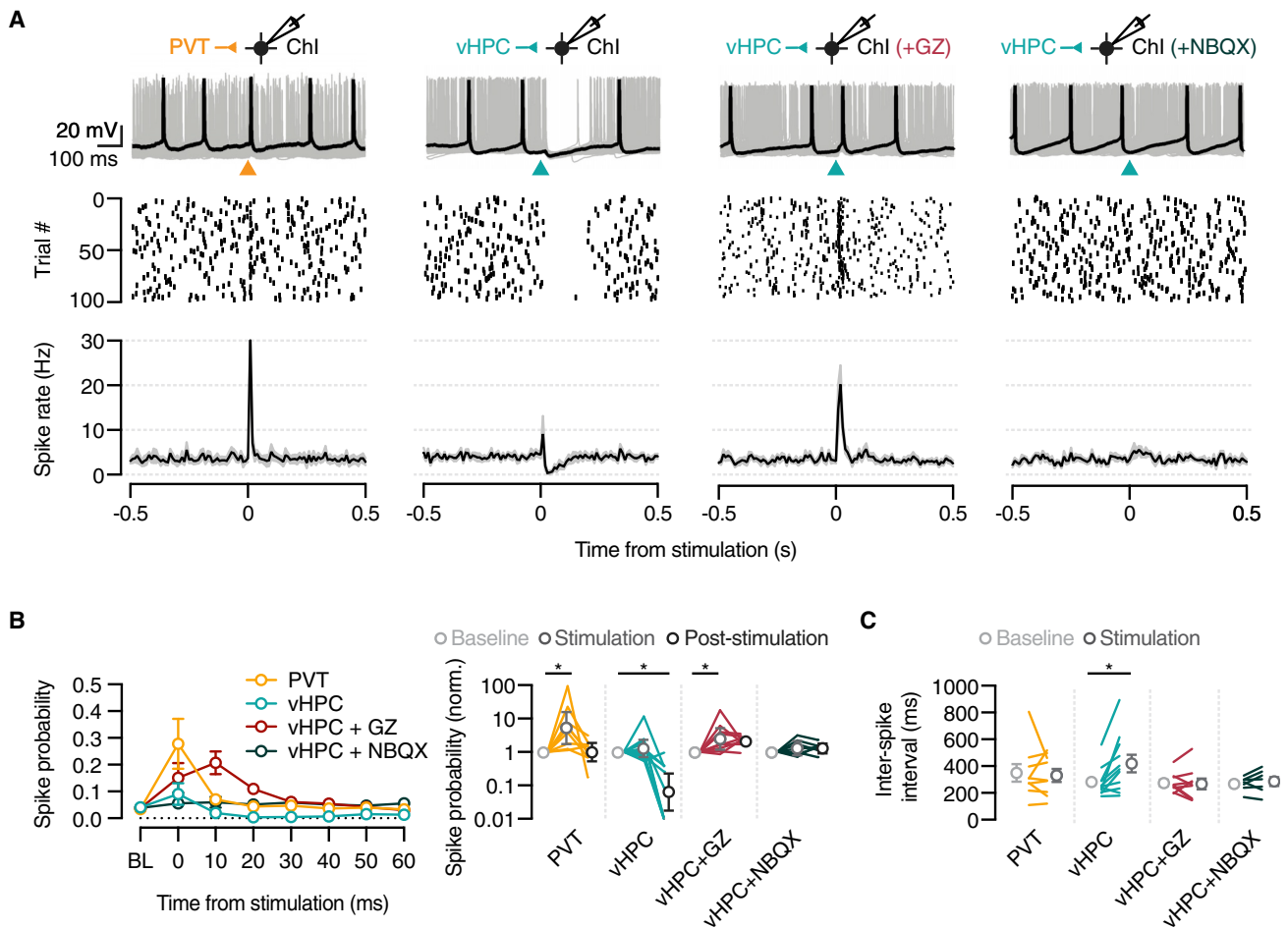


Figure 2. Contrasting impact of the PVT and vHPC on Chl firing

(A) Top: example current-clamp recording of Chls in response to PVT (orange) ($n = 8$ cells/6 mice), vHPC (teal) ($n = 11$ cells/9 mice), vHPC + gabazine (GZ) (red) ($n = 7$ cells/3 mice), and vHPC + NBQX (dark green) ($n = 7$ cells/3 mice) stimulation. Middle: raster plot of spike timing. Bottom: summary of spike rate across time. (B) Left: summary of effect of stimulation on spike probability (10 ms bins) for each recording condition. Right: summary of normalized spike probability relative to the pre-stimulus baseline (BL) (note log axis). Stimulation refers to the time from 0–10 ms and post-stimulation from 10–60 ms after optical stimulation. (C) Summary of effect of light stimulation on first inter-spike interval.

Average spike rate, spike probability, and inter-spike interval are presented as mean \pm SEM. Normalized spike probability data are presented as geometric mean with 95% confidence interval (CI) on a logarithmic axis. * $p < 0.05$.

See also [Figure S2](#).

observed in recordings of nearby putative MSNs in these slices ([Figure S3](#)). In contrast, equivalent activation of vHPC inputs evoked small EPSCs at -60 mV but large, delayed IPSCs at $+20$ mV ($n = 9$ cells/7 mice; EPSC amplitude: 107 ± 49 pA, IPSC amplitude: 649 ± 169 pA; Wilcoxon test: $W = 45.0$, $p = 0.004$; EPSC onset: 2.8 ± 0.4 ms, IPSC onset: 6.6 ± 0.4 ms; Wilcoxon test: $W = 26$, $p = 0.03$) ([Figures 3B and S3](#)). vHPC-evoked IPSCs were reliably blocked by gabazine and NBQX, confirming that they result from FFI (gabazine: EPSC amplitude = 62 ± 14 pA, IPSC amplitude = 4 ± 1 pA; Wilcoxon test: $W = -36$, $p = 0.008$; NBQX: EPSC amplitude = 3 ± 1 pA, IPSC amplitude = 5 ± 1 pA; Wilcoxon test: $W = 20$, $p = 0.1$) ([Figures 3C and S3](#)). These results suggest that PVT and vHPC differentially engage local inhibitory circuits in the NAcMS to modulate Chl activity.

We next sought to determine the source of vHPC-evoked FFI of Chls. Like the rest of the striatum, the NAc is composed almost entirely of GABAergic cells, including MSNs and multiple interneurons ([Kawaguchi, 1993](#); [Scudder et al., 2018](#); [Tepper and Bolam, 2004](#)). To determine which cells are engaged by the vHPC to drive inhibition onto Chls, we compared IPSC amplitudes in voltage-clamp recordings of Chls to action potential firing in current-clamp recordings of neighboring parvalbumin-expressing (PV+) cells ([Figure 3D](#)), dopamine type 1 receptor-expressing (D1+) MSNs ([Figure 3E](#)), or somatostatin-expressing (SOM+) cells ([Figure 3F](#)) with sequential paired recordings. D2+ MSNs were omitted because we have previously shown that vHPC inputs preferentially target and activate D1+ over D2+ MSNs ([Baimel et al., 2019](#); [MacAskill et al., 2012, 2014](#); [Scudder et al., 2018](#)). For each pair of neurons, we evoked glutamate release

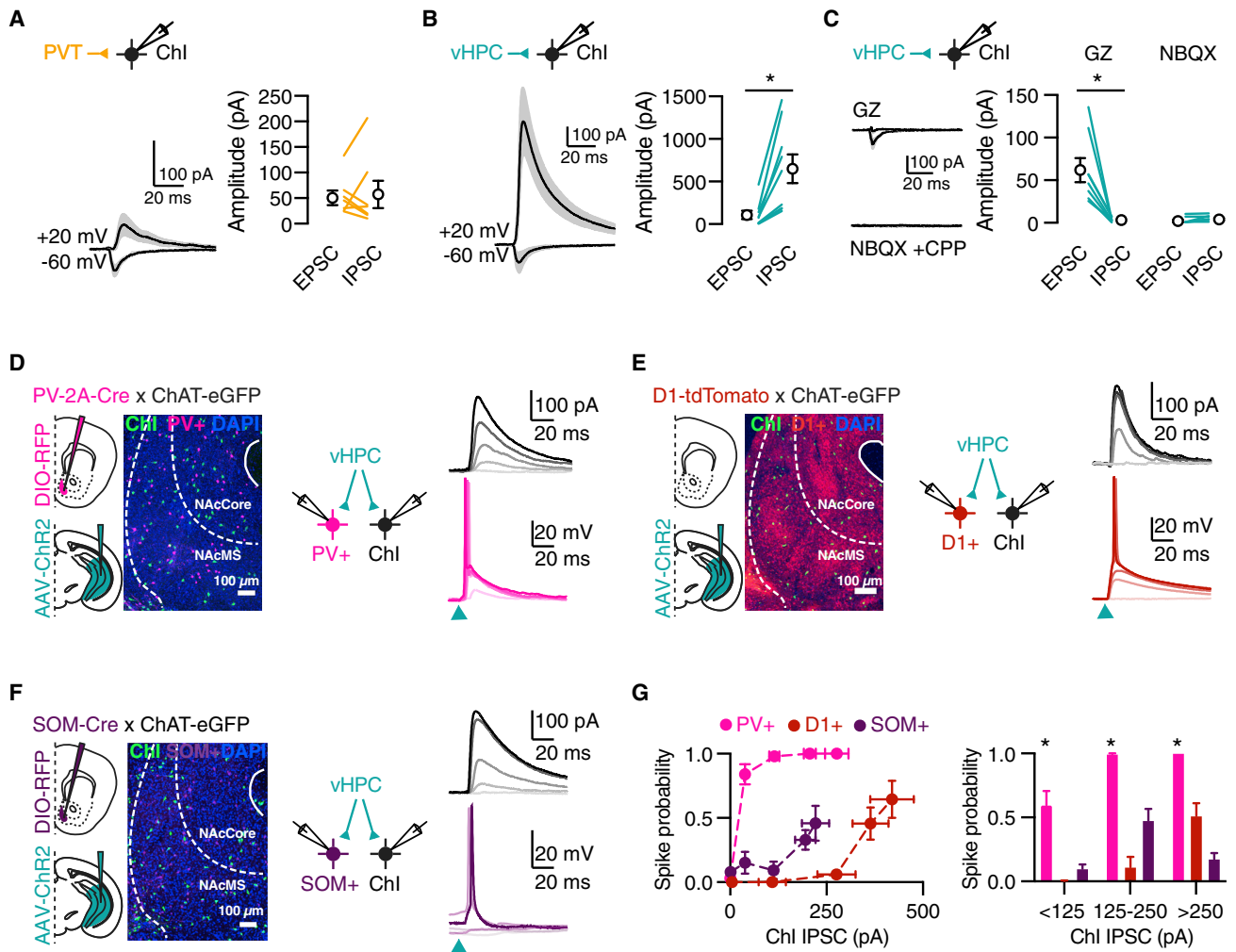


Figure 3. vHPC and PVT differentially recruit local inhibition

(A) Left: PVT-evoked EPSCs and IPSCs in ChIs. Right: summary of absolute amplitudes of PVT-evoked responses, where lines indicate individual neurons ($n = 7$ cells/4 mice).

(B) Similar to (A), showing prominent vHPC-evoked FFI ($n = 9$ cells/7 mice).

(C) Similar to (B), showing inhibition is blocked when gabazine (GZ) ($n = 8$ cells/5 mice) or NBQX ($n = 7$ cells/3 mice) are included in the bath.

(D) Left: schematic of injections of DIO-RFP in the NAcMS (pink) and AAV-ChR2 in the vHPC (teal) of a PV-2A-Cre \times ChAT-eGFP mouse. Middle: example image of the NAcMS illustrating PV+ interneurons (pink) and ChI labeling (green). Right: representative recordings for vHPC-evoked firing of PV+ interneurons (pink) in current clamp and IPSCs in a neighboring ChI (black) in voltage clamp. Firing and IPSCs were assessed at multiple light intensities, with relative intensity shown by the transition from light to dark colors ($n = 6$ cells/3 mice).

(E–F) Similar to (D) for D1-tdTomato \times ChAT-eGFP mice ($n = 6$ cells/3 mice) (E) and SOM-Cre \times ChAT-eGFP mice ($n = 5$ cells/3 mice) (F).

(G) Summary of evoked spike probabilities in PV+ (pink), D1+ (red), and SOM+ (purple) neurons relative to IPSC amplitude in ChIs (left) and binned by IPSC amplitude (right).

Average traces are presented as mean \pm SEM (A–C). For (D)–(F), example paired current- and voltage-clamp recordings are presented. Amplitude (A–C) and spike probability data (G) are presented as mean \pm SEM. * $p < 0.05$.

See also Figure S3.

from vHPC terminals, progressively increasing light intensity to drive more vHPC inputs (Figures 3D–3F) (Anastasiades et al., 2018). We found that brief stimulation of vHPC fibers readily fired PV+ interneurons at low light intensities, which corresponded to the emergence of IPSCs in ChIs (Figures 3D and 3G). In contrast, vHPC inputs only spiked D1+ MSNs and SOM+ interneurons at higher light intensities, well after the appearance of IPSCs in ChIs (Figures 3E–3G) (two-way ANOVA: IPSC amplitude \times cell-

type interaction, $F[4,96] = 3.52$, $p = 0.01$; Tukey's multiple comparisons: $p < 0.05$; $n = 6$ – 9 pairs from 3–5 mice per condition). Moreover, when comparing the onset times for spikes in PV+, SOM+, and D1+ neurons with the onset of IPSCs in ChIs, we found that PV+ interneurons were the only cells where action-potential onset preceded IPSC onset (Figure S3). Together, these results suggest that D1+ and SOM+ cells may contribute to vHPC-evoked FFI, but PV+ interneurons fire earlier and more

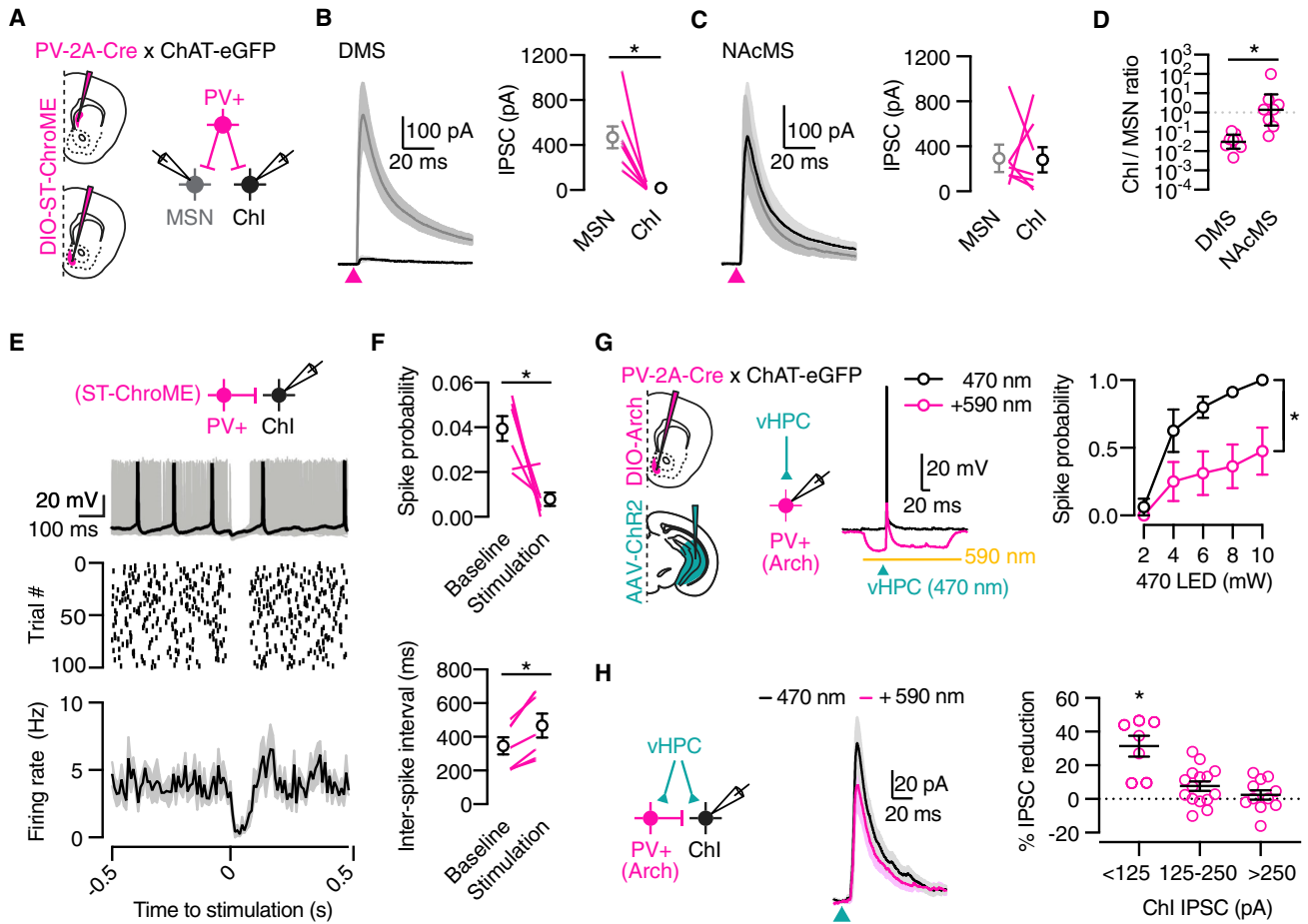


Figure 4. vHPC recruits PV+ interneurons to drive FFI onto ChIs

(A) Schematic of injections of DIO-ST-ChroME in the DMS (top) or NAcMS (bottom) of PV-2A-Cre x ChAT-eGFP mice. To assess synaptic connectivity in the local network, sequential-paired voltage-clamp recordings from a ChI and nearby MSN were made.

(B) Left: average PV+-evoked IPSCs in ChIs (black) or MSNs (grey) in the DMS. Right: summary of IPSC amplitudes in ChIs and MSNs, where lines represent individual pairs of neurons (n = 8 pairs/4 mice).

(C) Similar to (B) but for recordings in the NAcMS (n = 8 pairs/3 mice).

(D) Summary of ChI/MSN ratio for PV+-evoked IPSCs in the DMS and NAcMS.

(E) Top: schematic of recording condition and example current-clamp recording of ChIs in response to PV+ interneuron stimulation in the NAcMS. Middle: raster plot of spike timing. Bottom: summary of spike rate across time (n = 7 cells/3 mice).

(F) Top: summary of effect of PV+ stimulation on spike probability. Bottom: summary of effect of PV+ stimulation on inter-spike interval.

(G) Left: schematic of injections of AAV-DIO-ArchT in the NAcMS (pink) and AAV-ChR2 in the vHPC (teal) of PV-2A-Cre x ChAT-eGFP mice. Middle: example recording showing that activating ArchT with 590 nm light suppresses vHPC-evoked firing of PV+ interneurons. Right: summary of reduction in spike probability at different light intensities (n = 8 cells/4 mice).

(H) Left: schematic of recording conditions. Middle: average PV+-evoked IPSC amplitudes in ChIs for ChR2 alone (black) and ChR2+ArchT (pink) trials. Right: summary of ArchT-induced reduction in IPSC amplitude (n = 9 cells/4 mice).

Average traces are presented as mean ± SEM (B, C, and H). For (E) and (G), example current-clamp recordings are presented. Summary data are presented as mean ± SEM. Ratio data (D) are presented as geometric mean with 95% CI on a logarithmic axis. *p < 0.05.

See also Figure S4.

readily, and likely provide the initial source of inhibition to ChIs in the NAcMS.

FFI of ChIs is mediated by PV+ interneurons

At odds with these results, multiple studies in the dorsal striatum have failed to observe inhibition of ChIs by fast-spiking PV+ interneurons (Gittis et al., 2010; Straub et al., 2016; Szydlowski et al., 2013). We therefore hypothesized that there may be major

differences in the local circuit organization of dorsal and ventral striatum. To test this idea, we expressed the soma-tagged, Cre-dependent ChR2 variant ST-ChroME in the dorsal medial striatum (DMS) or NAcMS of PV-2A-Cre x ChAT-eGFP mice and performed sequential paired voltage-clamp recordings from neighboring ChIs and putative MSNs in slices (Figures 4A and S4). In the DMS, we confirmed previous reports of large PV+-driven IPSCs in MSNs, with little to no inhibition in ChIs

($n = 8$ pairs/4 mice; Chl: 20 ± 7 pA, MSN: 470 ± 96 pA; Wilcoxon test: $W = 36$, $p = 0.008$) (Figures 4B, 4D, and S4). In contrast, in the NAcMS, we observed robust IPSCs in both putative MSNs and Chls ($n = 8$ pairs/3 mice; Chl: 281 ± 111 pA, MSN: 295 ± 122 pA; Wilcoxon test: $W = -4$, $p = 0.8$) (Figures 4C, 4D, and S4), confirming that PV+ interneurons in the NAcMS make strong connections onto Chls. Although the specific MSN cell type was unknown to us here, in separate experiments, we confirmed robust targeting of D1+ and D1- MSNs, used as a proxy for D2+ MSNs, by PV+ interneurons (Figure S4) (Gittis et al., 2010; Scudder et al., 2018).

Having established the connectivity of PV+ cells in the NAcMS, we then tested if activation of these cells was sufficient to pause spiking in Chls. We again expressed ST-Chrome in PV+ interneurons in the NAcMS, now monitoring the effect of phasic activation on action-potential firing from Chls. We found that brief activation of PV+ interneurons robustly inhibited firing of Chls, which was associated with a pronounced decrease in spike probability (BL: 0.04 ± 0.006 , Stim: 0.008 ± 0.003 ; Wilcoxon test: $W = -26$, $p = 0.03$) and an increase in the inter-spike interval (BL: 342 ± 51 ms, Stim: 462 ± 71 ms; Wilcoxon test: $W = 28$, $p = 0.02$) (Figures 4E and 4F), indicating that PV+ interneurons robustly suppress the activity of Chls in the NAcMS.

Lastly, we directly tested the contribution of PV+ interneurons to FFI of Chls using optogenetic suppression. In PV-2A-Cre \times ChAT-eGFP mice, we expressed both Chr2 in the vHPC and the Cre-dependent inhibitory opsin ArchT in PV+ cells in the NAcMS (Figure 4G). This approach permitted simultaneous activation of vHPC inputs with blue (470 nm) light and suppression of PV+ firing with yellow (590 nm) light to test the role of PV+ interneurons in vHPC-evoked FFI. In control experiments, we first confirmed that activation of ArchT suppressed vHPC-evoked firing of PV+ interneurons (Kruskal-Wallis test with Dunn's multiple comparisons test: $H[2] = 10.35$, $p = 0.006$) (Figure 4G). We then made voltage-clamp recordings from Chls, evoking vHPC-induced feedforward IPSCs with multiple intensities of blue light and interleaved yellow light to activate ArchT. We found that inhibition of PV+ interneurons reduced vHPC-evoked feedforward IPSC amplitudes in Chls (Figure 4H). This effect was most prominent at small IPSC amplitudes, which are primarily driven by activation of PV+ interneurons (see Figure 3G) (IPSC < 125 pA: $31\% \pm 6\%$ reduction, IPSC = 125 – 250 pA: $8\% \pm 3\%$ reduction, IPSC > 250 pA: $2\% \pm 3\%$ reduction; $n = 9$ cells/4 mice; Kruskal-Wallis test with Dunn's multiple comparisons test: $H[2] = 10.35$, $p = 0.006$), confirming that these interneurons substantially contribute to FFI of Chls in the NAcMS.

DISCUSSION

Together, our findings help elucidate the long-range and local circuits that regulate the activity of Chls in the NAcMS. We show that Chls in this subregion of the NAc preferentially sample excitatory inputs from the PVT and the vHPC. Stimulation of PVT terminals evokes action potentials in Chls, while stimulation of vHPC inputs silences ongoing firing. This silencing reflects biased recruitment of local feedforward inhibitory circuits by the vHPC and involves the robust activation of PV+ interneurons, which make strong connections onto Chls in the NAcMS.

Recent studies have emphasized the importance of Chls in tracking and regulating NAc-dependent behavior (Al-Hasani et al., 2021; Brown et al., 2012) and their roles in addiction and other neuropsychiatric disorders (Lee et al., 2016; Warner-Schmidt et al., 2012; Witten et al., 2010), but the circuit mechanisms that govern the activity of these cells are not well defined. Our results indicate that Chls in the NAcMS are targeted by several populations of presynaptic neurons distributed across other brain regions. Monosynaptic excitatory inputs arrive primarily from the anterior PVT and the vHPC. In contrast, there is surprisingly little retrograde labeling in either the prefrontal cortex or the basolateral amygdala, both of which are well connected with D1+ and D2+ MSNs in the NAcMS (Baimel et al., 2019; Li et al., 2018; MacAskill et al., 2012, 2014; Pascoli et al., 2014), indicating selective targeting. We also identified inputs arriving from the anterior ventral pallidum but not the ventral tegmental area, despite both making strong inhibitory contacts onto Chls in the NAcMS (Al-Hasani et al., 2021; Brown et al., 2012; Vachez et al., 2021). The lack of labeling in the VTA could reflect a small population of presynaptic cells with widespread connectivity or may reflect a mismatch between our injection sites and the terminal field of VTA GABA neurons, which are densest in the most ventral portion of the NAcMS (Al-Hasani et al., 2021). Together, similar to other recent whole-brain rabies-tracing studies, these results suggest projection-specific regulation of interneurons in the striatum (Klug et al., 2018; Ribeiro et al., 2019), with Chls receiving a distinct set of afferents.

Although both the PVT and vHPC make excitatory, monosynaptic connections onto Chls, our results indicate that PVT inputs activate, while vHPC inputs suppress, ongoing activity in Chls. Because vHPC inputs are glutamatergic, their ability to evoke a prominent pause in Chl firing was particularly surprising. Pauses have been previously explained by dopaminergic modulation (Chuhma et al., 2014; Ding et al., 2010; Straub et al., 2016), intrinsic conductances (Oswald et al., 2009; Zhang et al., 2018), or long-range inhibitory inputs (Brown et al., 2012), but our data indicate a different mechanism. vHPC-evoked pauses were blocked when we included either gabazine or NBQX in the bath solution, indicating that the pause results from local FFI. We confirmed this with voltage-clamp recordings of robust IPSCs in Chls, which were much larger than EPSCs recorded in the same neurons. Like the pause in Chls, these IPSCs were blocked when we included gabazine or NBQX in the bath solution. This contrasts with PVT inputs, where feedforward IPSCs were smaller in amplitude and balanced by direct EPSCs recorded in the same cells. Interestingly, this does not seem to reflect an inability of PVT inputs to drive local inhibition but rather cell-type-specific interconnectivity in the NAcMS, as we observed larger PVT-evoked IPSCs in recordings of nearby MSNs in the same slices. Together, these results suggest that the vHPC and PVT make distinct synaptic connections in the NAcMS, leading to differential engagement of the local network and driving opposing regulation of Chls.

We establish PV+ interneurons as the main source of vHPC-evoked FFI onto Chls in the NAcMS. vHPC inputs reliably spike PV+ interneurons more readily and faster than other cell types in the NAcMS, which aligns with the emergence of IPSCs in Chls. This is consistent with some previous reports of strong

connections between the vHPC and PV+ interneurons (Scudder et al., 2018; Yu et al., 2017). However, it differs from several studies in the dorsal striatum, where fast-spiking PV+ interneurons evoke FFI at MSNs but show only weak and sparse connectivity at ChIs and other interneurons (Gittis et al., 2010; Straub et al., 2016; Szydlowski et al., 2013). Using soma-tagged optogenetics, we observed robust synaptic connectivity between PV+ interneurons and ChIs in the NAcMS. These inputs were sufficient to induce a pause-like response in tonically firing ChIs and necessary for vHPC-evoked feedforward IPSCs at ChIs. Our findings suggest a fundamentally different organization of local circuits in the dorsal and ventral striatum and represent a local mechanism for the induction of a pause-like response in ChIs in the NAcMS. Interestingly, vHPC inputs are most prominent in the NAcMS (Britt et al., 2012; MacAskill et al., 2012, 2014), suggesting that this mechanism may be restricted to this subregion. Relatedly, recent evidence highlights that VTA GABA neurons most reliably inhibit ChIs in the ventral portion of the NAcMS (Al-Hasani et al., 2021), suggesting that the regulation of ChIs is location dependent. In the future, it will be critical to determine the local and long-range connectivity of ChIs in the NAc core and lateral shell, which differentially sample long-range afferent inputs (Hunnicut et al., 2016; Li et al., 2018) and play distinct roles in behavior.

Lastly, our results have implications for how the vHPC and PVT drive functional signals via ChIs in the NAcMS. Throughout the striatum, pauses in ChI firing signal salience (Aosaki et al., 1994; Apicella et al., 2009; Ravel et al., 2003; Zhang and Cragg, 2017), enhance stimulus-outcome learning (Al-Hasani et al., 2021; Brown et al., 2012), and facilitate the learning of drug-context associations (Witten et al., 2010). Mechanistically, these pauses dampen cholinergic tone, which has prominent influence on modulating both local dopamine release (Cachope et al., 2012; Kosillo et al., 2016; Liu et al., 2022; Shin et al., 2015; Threlfell et al., 2012) and the activity of MSNs and other cell types in the local circuit (Assous et al., 2017; English et al., 2011; Koós and Tepper, 2002; Mamaligas and Ford, 2016; Oldenburg and Ding, 2012). By evoking FFI of ChIs, our results suggest that vHPC inputs contribute to learning processes by pausing ChI firing and initiating the downstream effects of decreased cholinergic tone in the NAcMS. However, this does not rule out a contribution of PVT inputs to salience signaling and stimulus-outcome learning. For example, NAc-projecting PVT neurons develop pronounced inhibitory responses to reward-predictive cues (Otis et al., 2019), which may act synergistically with vHPC inputs to enhance pause-like responses in ChIs. Moreover, PVT-evoked activation of ChIs may contribute to cue-driven increases in ChI activity and cholinergic tone, which develop specifically in the ventral NAcMS in response to reward-predicting cues (Al-Hasani et al., 2021). In the future, it will be important to determine when vHPC and PVT inputs are active in the intact brain during behavior and how their activation shapes ChI activity.

Together, our results highlight the circuit properties that govern ChI activity in the NAcMS, elucidate a potential substrate for hippocampal salience signaling within ventral striatum, and augment a growing literature that suggests that the separation of behavioral function across striatal subregions reflects region-specific connectivity rules.

Limitations of the study

While our results demonstrate a clear role for PV+ interneurons in vHPC-evoked inhibition of ChIs, we were unable to obtain complete suppression of feedforward IPSCs when inhibiting PV+ interneurons. The explanation for this could be both experimental and biological. Although we could potentially decrease vHPC-driven spikes in PV+ interneurons with activation of ArchT (Figure 4G), vHPC inputs are particularly strong onto PV+ interneurons (Scudder et al., 2018), and in some trials, we still observed spiking of PV+ interneurons during ArchT activation, which would contribute to feedforward IPSCs. Similarly, because the manipulations of PV+ interneurons depended on viral expression, it is possible that certain PV+ interneurons expressed insufficient levels of ArchT and were not properly inhibited in our experiments. Alternatively, recent advances show tremendous diversity of striatal interneurons (Chen et al., 2021; Dorst et al., 2020; Muñoz-Manchado et al., 2018; Tepper et al., 2018), and we cannot rule out a contribution of other striatal cell types.

Our findings also raise multiple questions for future study. Here, we characterized responses to the synchronous activation of vHPC or PVT inputs in a brain-slice preparation, where activity is largely quiescent and ongoing neuromodulation is broadly absent. Moving forward, it will be very important to determine how these synaptic mechanisms function and fluctuate *in vivo* and during active behavior, when synaptic connections and the overall NAc network are in different states.

STAR★METHODS

Detailed methods are provided in the online version of this paper and include the following:

- KEY RESOURCES TABLE
- RESOURCE AVAILABILITY
 - Lead contact
 - Materials availability
 - Data and code availability
- EXPERIMENTAL MODEL AND SUBJECT DETAILS
- METHOD DETAILS
 - Stereotaxic injections
 - Rabies virus tracing
 - Slice preparation
 - Electrophysiology
 - Optogenetics
 - Histology and fluorescence microscopy
- QUANTIFICATION & STATISTICAL ANALYSIS

SUPPLEMENTAL INFORMATION

Supplemental information can be found online at <https://doi.org/10.1016/j.celrep.2022.111042>.

ACKNOWLEDGMENTS

We thank the Carter lab, Margaret Rice, and Nicolas Tritsch for helpful discussions and comments on the manuscript. This work was supported by a Revson postdoctoral fellowship (C.B.), NIH F32 DA044691 (S.L.S.), and NIH R01

DA038138 (A.G.C.). The present address for S.L.S. is Department of Psychology, California State University, Dominguez Hills, Carson, CA 90747, USA.

AUTHOR CONTRIBUTIONS

C.B., E.J., S.L.S., and A.G.C. designed the experiments. C.B., E.J., and S.L.S. performed the experiments. C.B., E.J., and K.M. analyzed the data. C.B. and A.G.C. wrote the paper.

DECLARATION OF INTERESTS

The authors declare no competing interests.

Received: January 31, 2022

Revised: May 12, 2022

Accepted: June 12, 2022

Published: July 5, 2022

REFERENCES

- Ade, K.K., Wan, Y., Chen, M., Gloss, B., and Calakos, N. (2011). An improved BAC transgenic fluorescent reporter line for sensitive and specific identification of striatonigral medium spiny neurons. *Front. Syst. Neurosci.* 5, 32. <https://doi.org/10.3389/fnsys.2011.00032>.
- Al-Hasani, R., Gowrishankar, R., Schmitz, G.P., Pedersen, C.E., Marcus, D.J., Shirley, S.E., Hobbs, T.E., Elerding, A.J., Renaud, S.J., Jing, M., et al. (2021). Ventral tegmental area GABAergic inhibition of cholinergic interneurons in the ventral nucleus accumbens shell promotes reward reinforcement. *Nat. Neurosci.* 24, 1114–1428.
- Ambroggi, F., Ishikawa, A., Fields, H.L., and Nicola, S.M. (2008). Basolateral amygdala neurons facilitate reward-seeking behavior by exciting nucleus accumbens neurons. *Neuron* 59, 648–661. <https://doi.org/10.1016/j.neuron.2008.07.004>.
- Anastasiades, P.G., Marlin, J.J., and Carter, A.G. (2018). Cell-type specificity of callosally evoked excitation and feedforward inhibition in the prefrontal cortex. *Cell Rep.* 22, 679–692. <https://doi.org/10.1016/j.celrep.2017.12.073>.
- Aosaki, T., Tsubokawa, H., Ishida, A., Watanabe, K., Graybiel, A.M., Kimura, M., and Ishida, A. (1994). Responses of tonically active neurons in the primate's striatum undergo systematic changes during behavioral sensorimotor conditioning. *J. Neurosci.* 14, 3969–3984. <https://doi.org/10.1523/jneurosci.14-06-03969.1994>.
- Apicella, P., Deffains, M., Ravel, S., and Legallet, E. (2009). Tonic active neurons in the striatum differentiate between delivery and omission of expected reward in a probabilistic task context. *Eur. J. Neurosci.* 30, 515–526. <https://doi.org/10.1111/j.1460-9568.2009.06872.x>.
- Assous, M., Kaminer, J., Shah, F., Garg, A., Koós, T., and Tepper, J.M. (2017). Differential processing of thalamic information via distinct striatal interneuron circuits. *Nat. Commun.* 8, 15860.
- Baimel, C., McGarry, L.M., and Carter, A.G. (2019). The projection targets of medium spiny neurons govern cocaine-evoked synaptic plasticity in the nucleus accumbens. *Cell Rep.* 28, 2256–2263.e3. <https://doi.org/10.1016/j.celrep.2019.07.074>.
- Britt, J.P., Benaliouad, F., McDevitt, R.A., Stuber, G.D., Wise, R.A., and Bonci, A. (2012). Synaptic and behavioral profile of multiple glutamatergic inputs to the nucleus accumbens. *Neuron* 76, 790–803. <https://doi.org/10.1016/j.neuron.2012.09.040>.
- Brown, M.T.C., Tan, K.R., O'Connor, E.C., Nikonenko, I., Muller, D., and Lüscher, C. (2012). Ventral tegmental area GABA projections pause accumbal cholinergic interneurons to enhance associative learning. *Nature* 492, 452–456. <https://doi.org/10.1038/nature11657>.
- Cachope, R., Mateo, Y., Mathur, B.N., Irving, J., Wang, H.-L., Morales, M., Lovinger, D.M., and Cheer, J.F. (2012). Selective activation of cholinergic interneurons enhances accumbal phasic dopamine release: setting the tone for reward processing. *Cell Rep.* 2, 33–41. <https://doi.org/10.1016/j.celrep.2012.05.011>.
- Chen, R., Blosser, T.R., Djekidel, M.N., Hao, J., Bhattacharjee, A., Chen, W., Tuesta, L.M., Zhuang, X., and Zhang, Y. (2021). Decoding molecular and cellular heterogeneity of mouse nucleus accumbens. *Nat. Neurosci.* 24, 1757–1771. <https://doi.org/10.1038/s41593-021-00938-x>.
- Christoffel, D.J., Walsh, J.J., Heifets, B.D., Hoerbelt, P., Neuner, S., Sun, G., Ravikumar, V.K., Wu, H., Halpern, C.H., and Malenka, R.C. (2021). Input-specific modulation of murine nucleus accumbens differentially regulates hedonic feeding. *Nat. Commun.* 12, 2135. <https://doi.org/10.1038/s41467-021-22430-7>.
- Chuhma, N., Mingote, S., Moore, H., and Rayport, S. (2014). Dopamine neurons control striatal cholinergic neurons via regionally heterogeneous dopamine and glutamate signaling. *Neuron* 81, 901–912. <https://doi.org/10.1016/j.neuron.2013.12.027>.
- Collins, A.L., Aitken, T.J., Huang, I.-W., Shieh, C., Greenfield, V.Y., Monbouquette, H.G., Ostlund, S.B., and Wassum, K.M. (2019). Nucleus accumbens cholinergic interneurons oppose cue-motivated behavior. *Biol. Psychiatr.* 86, 388–396. <https://doi.org/10.1016/j.biopsych.2019.02.014>.
- Ding, J.B., Guzman, J.N., Peterson, J.D., Goldberg, J.A., and Surmeier, D.J. (2010). Thalamic gating of corticostriatal signaling by cholinergic interneurons. *Neuron* 67, 294–307. <https://doi.org/10.1016/j.neuron.2010.06.017>.
- Doig, N.M., Magill, P.J., Apicella, P., Bolam, J.P., and Sharott, A. (2014). Cortical and thalamic excitation mediate the multiphase responses of striatal cholinergic interneurons to motivationally salient stimuli. *J. Neurosci.* 34, 3107–3117.
- Dorst, M.C., Tokarska, A., Zhou, M., Lee, K., Stagkourakis, S., Broberger, C., Masmanidis, S., and Silberberg, G. (2020). Polysynaptic inhibition between striatal cholinergic interneurons shapes their network activity patterns in a dopamine-dependent manner. *Nat. Commun.* 11, 5113. <https://doi.org/10.1038/s41467-020-18882-y>.
- English, D.F., Ibanez-Sandoval, O., Stark, E., Tecuapetla, F., Buzsáki, G., Deisseroth, K., Tepper, J.M., and Koós, T. (2011). *Nat. Neurosci.* 15, 123–130.
- Faget, L., Zell, V., Souter, E., McPherson, A., Ressler, R., Gutierrez-Reed, N., Yoo, J.H., Dulcis, D., and Hnasko, T.S. (2018). Opponent control of behavioral reinforcement by inhibitory and excitatory projections from the ventral pallidum. *Nat. Commun.* 9, 849. <https://doi.org/10.1038/s41467-018-03125-y>.
- Gittis, A.H., Nelson, A.B., Thwin, M.T., Palop, J.J., and Kreitzer, A.C. (2010). Distinct roles of GABAergic interneurons in the regulation of striatal output pathways. *J. Neurosci.* 30, 2223–2234. <https://doi.org/10.1523/jneurosci.4870-09.2010>.
- Higley, M.J., Soler-Llavina, G.J., and Sabatini, B.L. (2009). Cholinergic modulation of multivesicular release regulates striatal synaptic potency and integration. *Nat. Neurosci.* 12, 1121–1128. <https://doi.org/10.1038/nn.2368>.
- Howe, M., Ridouh, I., Allegra Mascaro, A.L., Larios, A., Azcorra, M., and Dombeck, D.A. (2019). Coordination of rapid cholinergic and dopaminergic signaling in striatum during spontaneous movement. *Elife* 8, e44903. <https://doi.org/10.7554/elife.44903>.
- Hunnicutt, B.J., Jongbloets, B.C., Birdsong, W.T., Gertz, K.J., Zhong, H., and Mao, T. (2016). A comprehensive excitatory input map of the striatum reveals novel functional organization. *Elife* 5, e19103. <https://doi.org/10.7554/elife.19103>.
- Kawaguchi, Y. (1993). Physiological, morphological, and histochemical characterization of three classes of interneurons in rat neostriatum. *J. Neurosci.* 13, 4908–4923. <https://doi.org/10.1523/jneurosci.13-11-04908.1993>.
- Klug, J.R., Engelhardt, M.D., Cadman, C.N., Li, H., Smith, J.B., Ayala, S., Williams, E.W., Hoffman, H., and Jin, X. (2018). Differential inputs to striatal cholinergic and parvalbumin interneurons imply functional distinctions. *Elife* 7, e35657. <https://doi.org/10.7554/elife.35657>.
- Koós, T., and Tepper, J.M. (2002). Dual cholinergic control of fast-spiking interneurons in the neostriatum. *J. Neurosci.* 22, 529–535.
- Kosillo, P., Zhang, Y.-F., Threlfell, S., and Cragg, S.J. (2016). Cortical control of striatal dopamine transmission via striatal cholinergic interneurons. *Cerebr. Cortex* 26, 4160–4169. <https://doi.org/10.1093/cercor/bhw252>.

- Lapper, S.R., and Bolam, J.P. (1992). Input from the frontal cortex and the parafascicular nucleus to cholinergic interneurons in the dorsal striatum of the rat. *Neuroscience* 51, 533–545.
- Lee, J., Finkelstein, J., Choi, J.Y., and Witten, I.B. (2016). Linking cholinergic interneurons, synaptic plasticity, and behavior during the extinction of a cocaine-context association. *Neuron* 90, 1071–1085.
- Li, Z., Chen, Z., Fan, G., Li, A., Yuan, J., and Xu, T. (2018). Cell-type-specific afferent innervation of the nucleus accumbens core and shell. *Front. Neuroanat.* 12, 84. <https://doi.org/10.3389/fnana.2018.00084>.
- Little, J.P., and Carter, A.G. (2013). Synaptic mechanisms underlying strong reciprocal connectivity between the medial prefrontal cortex and basolateral amygdala. *J. Neurosci.* 33, 15333–15342. <https://doi.org/10.1523/jneurosci.2385-13.2013>.
- Liu, C., Cai, X., Ritzau-Jost, A., Kramer, P.F., Li, Y., Khaliq, Z.M., Hallermann, S., and Kaeser, P.S. (2022). An action potential initiation mechanism in distal axons for the control of dopamine release. *Science* 375, 1378–1385. <https://doi.org/10.1126/science.abn0532>.
- MacAskill, A.F., Cassel, J.M., and Carter, A.G. (2014). Cocaine exposure reorganizes cell type- and input-specific connectivity in the nucleus accumbens. *Nat. Neurosci.* 17, 1198–1207. <https://doi.org/10.1038/nn.3783>.
- MacAskill, A.F., Little, J.P., Cassel, J.M., and Carter, A.G. (2012). Subcellular connectivity underlies pathway-specific signaling in the nucleus accumbens. *Nat. Neurosci.* 15, 1624–1626. <https://doi.org/10.1038/nn.3254>.
- Madisen, L., Zwingman, T.A., Sunkin, S.M., Oh, S.W., Zariwala, H.A., Gu, H., Ng, L.L., Palmiter, R.D., Hawrylycz, M.J., Jones, A.R., et al. (2010). A robust and high-throughput cre reporting and characterization system for the whole mouse brain. *Nat. Neurosci.* 13, 133–140. <https://doi.org/10.1038/nn.2467>.
- Malenka, R.C., and Kocsis, J.D. (1988). Presynaptic actions of carbachol and adenosine on corticostriatal synaptic transmission studied in vitro. *J. Neurosci.* 8, 3750–3756. <https://doi.org/10.1523/jneurosci.08-10-03750.1988>.
- Mamaligas, A.A., and Ford, C.P. (2016). Spontaneous synaptic activation of muscarinic receptors by striatal cholinergic neuron firing. *Neuron* 91, 574–586. <https://doi.org/10.1016/j.neuron.2016.06.021>.
- Mark, G.P., Rada, P., Pothos, E., and Hoebel, B.G. (1992). Effects of feeding and drinking on acetylcholine release in the nucleus accumbens, striatum, and hippocampus of freely behaving rats. *J. Neurochem.* 58, 2269–2274. <https://doi.org/10.1111/j.1471-4159.1992.tb10973.x>.
- Muñoz-Manchado, A.B., Bengtsson Gonzales, C., Zeisel, A., Munguba, H., Bekkouche, B., Skene, N.G., Lönnerberg, P., Ryge, J., Harris, K.D., Linnarsson, S., and Hjerling-Leffler, J. (2018). Diversity of interneurons in the dorsal striatum revealed by single-cell RNA sequencing and patchseq. *Cell Rep.* 24, 2179–2190.e7. <https://doi.org/10.1016/j.celrep.2018.07.053>.
- Nougaret, S., and Ravel, S. (2015). Modulation of tonically active neurons of the monkey striatum by events carrying different force and reward information. *J. Neurosci.* 35, 15214–15226. <https://doi.org/10.1523/jneurosci.0039-15.2015>.
- Oldenburg, I.A., and Ding, J.B. (2012). Cholinergic modulation of synaptic integration and dendritic excitability in the striatum. *Curr. Opin. Neurobiol.* 21, 425–432. <https://doi.org/10.1016/j.conb.2011.04.004>.
- Oswald, M.J., Oorschot, D.E., Schulz, J.M., Lipski, J., and Reynolds, J.N.J. (2009). Ih current generates the afterhyperpolarisation following activation of subthreshold cortical synaptic inputs to striatal cholinergic interneurons. *J. Physiol.* 587, 5879–5897. <https://doi.org/10.1113/jphysiol.2009.177600>.
- Otis, J.M., Zhi, M., Nambodiri, V.M.K., Cook, C.A., Kosyk, O., Matan, A.M., Ying, R., Hashikawa, Y., Hashikawa, K., Trujillo-Pisanty, I., Guo, J., Ung, R.L., Rodriguez-Romaguera, J., Anton, E.S., and Stuber, G.D. (2019). Paraventricular thalamus projection neurons integrate cortical and hypothalamic signals for cue-reward processing. *Neuron* 103, 423–431.
- Pascoli, V., Terrier, J., Espallergues, J., Valjent, E., O'Connor, E.C., and Lüscher, C. (2014). Contrasting forms of cocaine-evoked plasticity control components of relapse. *Nature* 509, 459–464. <https://doi.org/10.1038/nature13257>.
- Peteanu, L., Mao, T., Sternson, S.M., and Svoboda, K. (2009). The subcellular organization of neocortical excitatory connections. *Nature* 457, 1142–1145. <https://doi.org/10.1038/nature07709>.
- Phillipson, O.T., and Griffiths, A.C. (1985). The topographic order of inputs to nucleus accumbens in the rat. *Neuroscience* 16, 275–296. [https://doi.org/10.1016/0306-4522\(85\)90002-8](https://doi.org/10.1016/0306-4522(85)90002-8).
- Ravel, S., Legallet, E., and Apicella, P. (2003). Responses of tonically active neurons in the monkey striatum discriminate between motivationally opposing stimuli. *J. Neurosci.* 23, 8489–8497. <https://doi.org/10.1523/jneurosci.23-24-08489.2003>.
- Reed, S.J., Lafferty, C.K., Mendoza, J.A., Yang, A.K., Davidson, T.J., Grose-nick, L., Deisseroth, K., and Britt, J.P. (2018). Coordinated reductions in excitatory input to the nucleus accumbens underlie food consumption. *Neuron* 99, 1260–1273.e4. <https://doi.org/10.1016/j.neuron.2018.07.051>.
- Ribeiro, E.A., Nectow, A.R., Pomeranz, L.E., Ekstrand, M.I., Koo, J.W., and Nestler, E.J. (2019). Viral labeling of neurons synaptically connected to nucleus accumbens somatostatin interneurons. *PLoS One* 14, e0213476. <https://doi.org/10.1371/journal.pone.0213476>.
- Scudder, S.L., Baimel, C., Macdonald, E.E., and Carter, A.G. (2018). Hippocampal-evoked feedforward inhibition in the nucleus accumbens. *J. Neurosci.* 38, 9091–9104. <https://doi.org/10.1523/jneurosci.1971-18.2018>.
- Sesack, S.R., and Grace, A.A. (2010). Cortico-basal ganglia reward network: microcircuitry. *Neuro. Pharmacol.* 35, 27–47. <https://doi.org/10.1038/npp.2009.93>.
- Shin, J.H., Adrover, M.F., Wess, J., and Alvarez, V.A. (2015). Muscarinic regulation of dopamine and glutamate transmission in the nucleus accumbens. *Proc. Natl. Acad. Sci. USA* 112, 8124–8129. <https://doi.org/10.1073/pnas.1508846112>.
- Straub, C., Saulnier, J.L., Bègue, A., Bègue, A., Feng, D.D., Huang, K.W., and Sabatini, B.L. (2016). Principles of synaptic organization of GABAergic interneurons in the striatum. *Neuron* 92, 84–92. <https://doi.org/10.1016/j.neuron.2016.09.007>.
- Straub, C., Tritsch, N.X., Hagan, N.A., Gu, C., and Sabatini, B.L. (2014). Multiphasic modulation of cholinergic interneurons by nigrostriatal afferents. *J. Neurosci.* 34, 8557–8569. <https://doi.org/10.1523/jneurosci.0589-14.2014>.
- Sugita, S., Uchimura, N., Jiang, Z.G., and North, R.A. (1991). Distinct muscarinic receptors inhibit release of gamma-aminobutyric acid and excitatory amino acids in mammalian brain. *Proc. Natl. Acad. Sci. USA* 88, 2608–2611. <https://doi.org/10.1073/pnas.88.6.2608>.
- Szydlowski, S.N., Pollak Dorocic, I., Planert, H., Carlén, M., Meletis, K., and Silberberg, G. (2013). Target selectivity of feedforward inhibition by striatal fast-spiking interneurons. *J. Neurosci.* 33, 1678–1683. <https://doi.org/10.1523/jneurosci.3572-12.2013>.
- Taniguchi, H., He, M., Wu, P., Kim, S., Paik, R., Sugino, K., Kvitsani, D., Fu, Y., Lu, J., Lin, Y., et al. (2011). A resource of cre driver lines for genetic targeting of GABAergic neurons in cerebral cortex. *Neuron* 71, 995–1013. <https://doi.org/10.1016/j.neuron.2011.07.026>.
- Tepper, J.M., and Bolam, J.P. (2004). Functional diversity and specificity of neostriatal interneurons. *Curr. Opin. Neurobiol.* 14, 685–692. <https://doi.org/10.1016/j.conb.2004.10.003>.
- Tepper, J.M., Koós, T., Ibanez-Sandoval, O., Tecuapetla, F., Faust, T.W., and Assoum, M. (2018). Heterogeneity and diversity of striatal GABAergic interneurons: update 2018. *Front Neuroanat* 12, 91.
- Threlfell, S., Lalic, T., Platt, N.J., Jennings, K.A., Deisseroth, K., and Cragg, S.J. (2012). Striatal dopamine release is triggered by synchronized activity in cholinergic interneurons. *Neuron* 75, 58–64. <https://doi.org/10.1016/j.neuron.2012.04.038>.
- Tooley, J., Marconi, L., Alipio, J.B., Matikainen-Ankney, B., Georgiou, P., Kravitz, A.V., and Creed, M.C. (2018). Glutamatergic ventral pallidal neurons modulate activity of the habenula - tegmental circuitry and constrain reward seeking. *Biol. Psychiatr.* 83, 1012–1023. <https://doi.org/10.1016/j.biopsych.2018.01.003>.

- Vachez, Y.M., Tooley, J.R., Abiraman, K., Matikainen-Ankney, B., Casey, E., Earnest, T., Ramos, L.M., Silberberg, H., Godynuk, E., Uddin, O., et al. (2021). Ventral arkypallidal neurons inhibit accumbal firing to promote reward consumption. *Nat. Neurosci.* *24*, 379–390. <https://doi.org/10.1038/s41593-020-00772-7>.
- Virk, M.S., Sagi, Y., Medrihan, L., Leung, J., Kaplitt, M.G., and Greengard, P. (2016). Opposing roles for serotonin in cholinergic neurons of the ventral and dorsal striatum. *Proc. Natl. Acad. Sci. USA* *113*, 734–739. <https://doi.org/10.1073/pnas.1524183113>.
- Wall, N.R., Wickersham, I.R., Cetin, A., De La Parra, M., and Callaway, E.M. (2010). Monosynaptic circuit tracing in vivo through Cre-dependent targeting and complementation of modified rabies virus. *Proc. Natl. Acad. Sci. USA* *107*, 21848–21853. <https://doi.org/10.1073/pnas.1011756107>.
- Wang, Q., Ding, S., Li, Y., Royall, J., Feng, D., Lesnar, P., Graddis, N., Naeemi, M., Facer, B., Ho, A., et al. (2020). The Allen mouse brain common coordinate framework: a 3D reference atlas. *Cell* *181*, 936–953.e20. <https://doi.org/10.1016/j.cell.2020.04.007>.
- Warner-Schmidt, J.L., Schmidt, E.F., Marshall, J.J., Rubin, A.J., Arrango-Lievano, M., Kaplitt, M.G., Ibañez-Tallon, I., Heintz, N., and Greengard, P. (2012). Cholinergic interneurons in the nucleus accumbens regulate depression-like behavior. *Proc Natl Acad Sci USA* *109*, 11360–11365.
- Wilson, C.J., Chang, H.T., and Kitai, S.T. (1990). Firing patterns and synaptic potentials of identified giant aspiny interneurons in the rat neostriatum. *J. Neurosci.* *10*, 508–519. <https://doi.org/10.1523/jneurosci.10-02-00508.1990>.
- Witten, I.B., Lin, S.-C., Brodsky, M., Prakash, R., Diester, I., Anikeeva, P., Gradinaru, V., Ramakrishnan, C., and Deisseroth, K. (2010). Cholinergic interneurons control local circuit activity and cocaine conditioning. *Science* *330*, 1677–1681. <https://doi.org/10.1126/science.1193771>.
- Yu, J., Yan, Y., Li, K.-L., Wang, Y., Huang, Y.H., Urban, N.N., Nestler, E.J., Schlüter, O.M., and Dong, Y. (2017). Nucleus accumbens feedforward inhibition circuit promotes cocaine self-administration. *Proc. Natl. Acad. Sci. USA* *114*, E8750–E8759. <https://doi.org/10.1073/pnas.1707822114>.
- Zhang, Y.-F., and Cragg, S.J. (2017). Pauses in striatal cholinergic interneurons: what is revealed by their common themes and variations? *Front. Syst. Neurosci.* *11*, 80. <https://doi.org/10.3389/fnsys.2017.00080>.
- Zhang, Y.-F., Reynolds, J.N.J., and Cragg, S.J. (2018). Pauses in cholinergic interneuron activity are driven by excitatory input and delayed rectification, with dopamine modulation. *Neuron* *98*, 918–925.e3. <https://doi.org/10.1016/j.neuron.2018.04.027>.
- Zhu, Y., Wienecke, C.F.R., Nachtrab, G., and Chen, X. (2016). A thalamic input to the nucleus accumbens mediates opiate dependence. *Nature* *530*, 219–222. <https://doi.org/10.1038/nature16954>.

STAR★METHODS

KEY RESOURCES TABLE

REAGENT or RESOURCE	SOURCE	IDENTIFIER
Bacterial and virus strains		
AAV1-CaMKIIa-ChR2-mCherry	Addgene	26975-AAV1
AAV9-CAG-DIO-ChroME.ST-p2A-H2B-mRuby3	Addgene	108912-AAV9
AAV1-EF1a-DIO-EYFP	Penn Vector Core	AV-1-27056
AAV9-FLEX-ArchT-GFP	UNC Vector Core	N/A
AAV1-EF1a-FLEX-TVA-Cherry	UNC Vector Core	N/A
AAV9-CAG-FLEX-oG	Salk	N/A
SADΔG-GFP(EnvA)	Salk	N/A
Chemicals, peptides, and recombinant proteins		
Biocytin	Sigma-Aldrich	Cat # B1758
Streptavidin-647	Invitrogen	Cat # S21374
CPP	Tocris	Cat # 0247
TTX	Tocris	Cat # 1069
4-AP	Tocris	Cat # 0940
NBQX	Tocris	Cat # 1044
Gabazine	Tocris	Cat # 1262
TEA	Tocris	Cat # 3068
QX-314	Tocris	Cat # 2313
VectaShield with DAPI	Vector Labs	RRID: AB_2336790
EGTA	Fluka	Cat # 03379
HEPES	Sigma-Aldrich	Cat # H3375
Experimental models: Organisms/strains		
Mouse: ChAT-Cre	Jackson Lab	RRID: IMSR_JAX:006410
Mouse: ChAT-eGFP	Jackson Lab	RRID: IMSR_JAX_007902
Mouse: C57BL/6J	Jackson Lab	RRID: IMSR_JAX:000664
Mouse: D1-tdTomato	Jackson Lab	RRID: IMSR_JAX:016204
Mouse: PV-2A-Cre	Jackson Lab	RRID: IMSR_JAX:012358
Mouse: SOM-Cre	Jackson Lab	RRID: IMSR_JAX:013044
Software and algorithms		
Igor Pro	WaveMetrics	RRID: SCR_000325
MATLAB	MathWorks	RRID: SCR_001622
Prism	GraphPad Software	RRID: SCR_002798

RESOURCE AVAILABILITY

Lead contact

Further information and requests for resources and reagents should be directed to and will be fulfilled by the lead contact, Adam Carter (adam.carter@nyu.edu).

Materials availability

This study did not generate new unique reagents.

Data and code availability

- All data reported in this paper will be shared by the [lead contact](#) upon request.
- This paper does not report original code

- Any additional information required to analyze the data reported in this paper is available from the [lead contact](#) upon request.

EXPERIMENTAL MODEL AND SUBJECT DETAILS

Monosynaptic input tracing was performed in choline acetyltransferase (ChAT) bacterial artificial chromosome (BAC) Cre mice (ChAT-Cre) (Jackson Laboratories, stock # 006410) and physiology experiments were performed in acute slices from ChAT(BAC)-eGFP mice (Jackson Laboratories, stock # 007902) crossed with either wild-type C57BL/6J mice (originally purchased from Jackson Laboratories), D1-tdTomato hemizygous BAC transgenic mice (Ade et al., 2011) (Jackson Laboratories, stock # 016204), PV-2A-Cre mice (Madisen et al., 2010) (Jackson Laboratories, stock # 012358) or SOM-Cre mice (Taniguchi et al., 2011) (Jackson Laboratories, stock # 013044). For all experiments both sexes were used, and mice were aged P42-P75. No animals had been involved in previous procedures. Animals were group-housed with same-sex littermates in a dedicated animal care facility and were maintained on a 12-h light/dark cycle with food and water given *ad libitum*. All procedures were conducted in accordance with guidelines approved by the New York University animal welfare committee.

METHOD DETAILS

Stereotaxic injections

Stereotaxic injections were performed on P33-P50 mice. Mice were anesthetized with isoflurane and head fixed in a stereotax (Kopf Instruments). A small craniotomy was made over the injection site, through which viruses were injected. Injection site coordinates were determined relative to bregma (mediolateral axis, dorsoventral axis, and rostrocaudal axis (in mm): NAcMS = -1.7 , -4.4 , $+1.6$ at a 14° angle; DMS = -1.7 , -3.0 , $+1.6$ at a 14° angle; vHPC = -3.0 , -4.6 and -3.6 , -3.0 ; PVT = -0.1 , -3.5 , -0.8 . Borosilicate pipettes with 5–10 μm tip diameters were backfilled and 100–360 nL was pressure-injected using a Nanoject III (Drummond) with 45–60 s inter-injection intervals. Pipettes were left in place for at least 10 min after injection before being slowly withdrawn. Optogenetic stimulation of PVT and vHPC terminals was achieved 18–21 days after injections of AAV1-CaMKIIa-ChR2-mCherry (Addgene, 26975-AAV1) into these regions. To activate PV + interneurons, AAV9-CAG-DIO-ChroME.ST-p2A-H2B-mRuby3 (Addgene, 108912-AAV9) was injected and given 7–9 days for expression. Optogenetic inhibition was achieved with injections of AAV9-FLEX-ArchT-GFP (UNC Vector Core). For ArchT experiments, two separate injections were performed. AAV1-CaMKIIa-ChR2-mCherry was injected into the vHPC and then 10 days later AAV9-FLEX-ArchT-GFP was injected and allowed to express for 11 days. This was necessary to restrict blue light activation of ArchT, which was found to occur with longer expression times. In some experiments, PV+ and SOM + interneurons were labeled with injections of the Cre-dependent fluorophore virus AAV1-EF1a-DIO-EYFP (Penn Vector Core, AV-1-27056). After all injections, animals were returned to their home cages before being used for experiments.

Rabies virus tracing

For monosynaptic rabies virus tracing, the helper viruses AAV1-EF1a-FLEX-TVA-Cherry (130 nL) (UNC Vector Core) and AAV9-CAG-FLEX-oG (450 nL) (Salk) were injected into a single hemisphere of the NAcMS of ChAT-Cre mice. After allowing 5 weeks for expression, 750 nL of SAD Δ G-GFP(EnvA) rabies virus (Salk) was injected at the same location. Mice were then left for an additional 7 days to allow for monosynaptic retrograde labeling, before being perfused, and brain slices prepared for fluorescent microscopy.

Slice preparation

Mice were anesthetized with an intraperitoneal injection of a lethal dose of ketamine/xylazine and perfused intracardially with an ice-cold cutting solution containing the following (in mM): 65 sucrose, 76 NaCl, 25 NaHCO₃, 1.4 NaH₂PO₄, 25 glucose, 2.5 KCl, 7 MgCl₂, 0.4 Na-ascorbate, and 2 Na-pyruvate (bubbled with 95% O₂/5% CO₂). 300 μm coronal sections were cut in this solution and transferred to artificial cerebral spinal fluid (ACSF) containing the following (in mM): 120 NaCl, 25 NaHCO₃, 1.4 NaH₂PO₄, 21 glucose, 2.5 KCl, 2 CaCl₂, 1 MgCl₂, 0.4 Na-ascorbate, and 2 Na-pyruvate (bubbled with 95% O₂/5% CO₂). Slices recovered for 30 min at 35°C and then were stored for at least 30 min at 24°C prior to recording. All experiments were conducted at 30–32°C.

Electrophysiology

Whole-cell patch clamp recordings were made from fluorescently identified ChIs, PV+ and SOM + interneurons, and D1+ MSNs in the NAcMS, located 300–600 μm medial to the anterior commissure. D1- MSNs were identified by the lack of tdTomato fluorescence in D1-tdTomato mice, and in some cases putative MSNs were identified by a lack of fluorescence in ChAT-eGFP mice. Where applicable, neurons were recorded in sequential pairs (ChI x PV+, ChI x D1+, ChI x SOM+, ChI x MSN, D1+ x D1-), where cells were located at the same depth in the slice and within 50 μm of each other (Baimel et al., 2019; MacAskill et al., 2012, 2014; Scudder et al., 2018). Recording order was varied between cell types within a given pair. For voltage-clamp experiments, borosilicate pipettes (3–5 M Ω) were filled with a Cs-based internal (in mM: 130 Cs-gluconate, 10 HEPES, 10 Na-phosphocreatine, 4 Mg₂-ATP, 0.4 NaGTP, 10 TEA, 2 QX-314, and 10 EGTA, pH 7.3 with CsOH). For current-clamp recordings, pipettes were filled with a K-based internal (in mM: 135 K-gluconate, 7 KCl, 10 HEPES, 10 Na-phosphocreatine, 4 Mg₂-ATP, 0.3 NaGTP, and 0.5 EGTA, pH 7.3 with KOH). In

some experiments, 5% biocytin was also included in the recording internal solution. All voltage-clamp recordings were made with 10 μ M CPP in the bath solution to block NMDA receptors, and in some experiments, 1 μ M TTX was included to block action potentials, along with 0.1 mM 4-AP and 4 mM external Ca^{2+} to restore presynaptic glutamate release. Cells were held at -60 mV to measure AMPAR-mediated excitatory currents, and at $+20$ mV to measure GABA_A-mediated inhibitory currents. Intrinsic properties of ChIs were assessed in current-clamp recordings made with 10 μ M CPP, 10 μ M gabazine, 10 μ M NBQX to block NMDARs, GABA_ARs and AMPARs, respectively. Current steps were applied to cells from a holding potential set to -50 mV. Input resistance was calculated using a -50 pA current injection. Afferent-evoked changes in ChI firing were assessed in spontaneously active ChIs in the NAcMS with whole-cell current-clamp recordings. For these recordings, ChIs were sufficiently depolarized to maintain baseline firing around 5 Hz. In some recordings, gabazine or NBQX were included in the bath solution. All chemicals were purchased from Tocris Bioscience or Sigma.

Electrophysiological data were collected using a MultiClamp 700B (Axon Instruments), signals were sampled at 10 kHz, and filtered at 2 kHz for voltage-clamp and 5 kHz for current-clamp recordings. Series resistance was monitored, less than 25 M Ω , and not compensated.

Optogenetics

Glutamate release was triggered by activating channelrhodopsin-2 (ChR2) present in presynaptic terminals of vHPC or PVT inputs in the NAcMS, or in the cell bodies of PV + interneurons. Presynaptic release was obtained with 2 ms pulses of 470 nm light from a blue light-emitting diode (LED; 470 nm; Thorlabs) through a 10 \times 0.3 NA immersion objective (Olympus) with a power range of 2–10 mW measured at the back focal plane of the objective. ArchT mediated suppression was achieved with yellow light (590 nm, 10 mW) delivered 50 ms before blue light stimulation of ChR2 through the same objective.

Histology and fluorescence microscopy

Mice were anesthetized and perfused intracardially with 0.01 M PBS followed by 4% PFA. Brains were stored in 4% PFA for 12–18 h at 4°C before being washed three times in 0.01 M PBS. Slices were cut on a VT-1000S vibratome (Leica) at 70 μ m thickness and directly mounted onto gel-coated glass slides, or at 40 μ m for biocytin-filled cells, which were stained with streptavidin conjugated Alexa 647. Slices were cover-slipped using VectaShield with DAPI (Vector Labs). Fluorescent images were taken on an Olympus VS120 microscope, using a 10 \times 0.25NA objective (Olympus) or a Leica TCS SP8 confocal microscope, using a 20 \times 0.75NA and 40 \times 1.3NA objective (Leica). All images were processed using NIH ImageJ.

QUANTIFICATION & STATISTICAL ANALYSIS

All electrophysiology and anatomical data were collected from a minimum of 3 animals, from different litters. Experimenters were not blind to experimental groups. No pre-test analyses were used to estimate sample sizes. No data were excluded from final analyses. For monosynaptic input data, brain slices were aligned to the Allen Common Coordinate Framework (Wang et al., 2020) and cell bodies were manually counted for slices from rostral-caudal coordinates $+2.6$ to -4.8 relative to Bregma. Presynaptic input regions were determined relative to the Allen Brain Atlas. Electrophysiology data were acquired using custom software in MATLAB (MathWorks) and were analyzed with IgorPro (WaveMetrics) and MATLAB. EPSC and IPSC amplitudes were averaged from a 1 ms window around the peak current for AMPAR EPSCs and GABA_A IPSCs. Average traces of synaptic currents in figures depict mean \pm SEM. For current clamp experiments, spikes were grouped in 10 ms bins, and current step or light-evoked changes in spike probability or inter-event interval were assessed by comparing to the pre-stimulus baseline. Statistical significance of differences was evaluated using the Wilcoxon Signed-Rank test for paired data, the Friedman test with Dunn's multiple comparisons test for data with multiple time points or with repeated measure 2-way ANOVA followed by Tukey or Sidak's multiple comparison with p values <0.05 considered significant. Image analysis was conducted using NIH ImageJ. Statistical tests and graph generation were performed using Prism 9 (GraphPad). Normalized data are displayed in figures on logarithmic axes with the geometric mean $\pm 95\%$ confidence interval.